



Universiteit
Leiden
The Netherlands

A molecular journey : tales of sublimating ices from hot cores to comets
Bogelund, E.G.

Citation

Bogelund, E. G. (2019, March 14). *A molecular journey : tales of sublimating ices from hot cores to comets*. Retrieved from <https://hdl.handle.net/1887/69725>

Version: Not Applicable (or Unknown)

License: [Licence agreement concerning inclusion of doctoral thesis in the Institutional Repository of the University of Leiden](#)

Downloaded from: <https://hdl.handle.net/1887/69725>

Note: To cite this publication please use the final published version (if applicable).

Cover Page



Universiteit Leiden



The handle <http://hdl.handle.net/1887/69725> holds various files of this Leiden University dissertation.

Author: Bogelund, E.G.

Title: A molecular journey : tales of sublimating ices from hot cores to comets

Issue Date: 2019-03-14



4

**Molecular complexity
on disk-scales
uncovered by ALMA:
The chemical
composition of the
high-mass protostar
AFGL 4176**

**E. G. Bøgelund, A. G. Barr, V. Taquet,
N. F. W. Ligterink, M. V. Persson,
M. R. Hogerheijde and E. F. van Dishoeck**

Submitted to Astronomy & Astrophysics

Abstract

Context. The chemical composition of high-mass protostars reflects the physical evolution associated with different stages of star formation. In addition, the spatial distribution and velocity structure of different molecular species provide valuable information of the physical structure of these embedded objects. However, so far most studies of these sources have been carried out using single-dish telescopes whose limited spatial resolution probe mainly the large-scale structure of the objects.

Aim. The molecular inventory of the forming high-mass star AFGL 4176, located at a distance of ~ 3.7 kpc, is studied in detail at high angular resolution of $\sim 0.35''$, equivalent to ~ 1285 au at the distance of AFGL 4176. This high resolution makes it possible to separate the emission associated with the inner hot envelope and disk around the forming star from that of its cool outer envelope. The composition of AFGL 4176 is compared with other, both high- and low-mass sources, and placed in the broader context of star-formation.

Methods. Using the Atacama Large Millimeter/submillimeter Array (ALMA) the chemical inventory of AFGL 4176 is characterised. The high sensitivity of ALMA makes it possible to identify weak and optically thin lines and allows for many isotopologues to be detected, providing a more complete and accurate inventory of the source. For the detected species, excitation temperatures in the range 120–320 K are determined and column densities are derived assuming LTE and using optically thin lines. The spatial distribution of a number of species is studied.

Results. A total of 354 lines is identified towards AFGL 4176 with a signal-to-noise ratio of three or higher. Of these lines, 324 can be assigned to 23 different molecular species and their isotopologues. The most abundant species is methanol (CH_3OH) with a column density of $5.5 \times 10^{18} \text{ cm}^{-2}$ in a beam of $\sim 0.3''$, derived from its ^{13}C -isotopologue. The remaining species are present at levels between 0.003 % and 15 % with respect to methanol. Hints that N-bearing species peak slightly closer to the location of the peak continuum emission than the O-bearing species are seen. A single species, propyne ($\text{CH}_3\text{C}_2\text{H}$), displays a double-peaked distribution.

Conclusions. AFGL 4176 comprises a rich chemical inventory including many complex species present on disk-scales. On average, the derived column density ratios with respect to methanol of O-bearing species are higher than those derived for N-bearing species by a factor of three. This may indicate that AFGL 4176 is a relatively young source since nitrogen chemistry generally takes longer to evolve in the gas-phase. Taking methanol as a reference, the composition of AFGL 4176 more closely resembles that of the low-mass protostar IRAS 16293–2422B than that of high-mass star-forming regions located near the Galactic centre. This similarity indicates that the production of complex species does not depend strongly on the luminosity of sources, but may be universal despite differences in physical conditions, or that the composition of species is set already in the ice during the cold cloud stage.

4.1 Introduction

The molecular composition of a star-forming region can be used to probe the physical conditions of its environment, define its evolutionary stage, identify chemical processes and in addition, sets the stage and starting conditions for chemistry in disks and eventually planetary systems. A large number of molecular species, ranging from simple to complex, that is molecules consisting of six or more atoms, have been identified in various interstellar environments, from giant molecular clouds to dense cores, protostars and protoplanetary disks (see reviews by Herbst & van Dishoeck, 2009; Caselli & Ceccarelli, 2012; Tielens, 2013; Sakai & Yamamoto, 2013). In context to the formation of high- and low-mass stars, the hot core or hot corino stage displays a particular rich chemistry. At this stage, the young protostar heats its surroundings and creates a bubble of warm (~ 200 K) gas, enriched in complex molecules. This complexity is a result of chemistry in the warm gas combined with thermal desorption of the icy mantles of dust grains (e.g. Charnley et al., 1992).

Over the last decades, many surveys, mostly using single-dish telescopes, have been undertaken to investigate the chemical complexity of high-mass hot cores (e.g. Blake et al., 1987; Hatchell et al., 1998; van der Tak et al., 2000; Ikeda et al., 2001; Bisschop et al., 2007; Isokoski et al., 2013; Suzuki et al., 2018). Much focus has been on the hot cores associated with Orion and Sagittarius B2 (hereafter Sgr B2), famous for their high abundances of complex molecules (see e.g. Neill et al., 2014; Crockett et al., 2014, and references therein), although recently, the low-mass counterparts of these sources have also been under investigations (e.g. Schöier et al., 2002; Cazaux et al., 2003; Bottinelli et al., 2004). A wealth of information on the chemistry associated with hot cores has been provided by these observations, although most are limited by the, in general, large beam sizes of single-dish telescopes. The consequence hereof is that observations do not only sample the hot core, but also the surrounding environments associated with the protostar, such as the large-scale envelope or outflows (e.g. Fayolle et al., 2015). Generally, this results in multi-component molecular emission, where each component may be characterised by a different line width, velocity, excitation temperature and column density. Furthermore, beam dilution effects may result in large uncertainties on derived molecular column densities if not accounted for correctly.

The emergence of interferometers such as the Submillimeter Array (SMA), the NOthern Extended Millimeter Array (NOEMA) and, in particular, the Atacama Large Millimeter/submillimeter Array (ALMA), which provide much higher spatial resolutions than single-dish telescopes, has made it possible to study the molecular emission associated with hot cores on much smaller scales than were previously accessible. This means, that for the first time, an opportunity to "look into" the hot cores themselves is provided whereby the challenges of many single-dish studies can be overcome. In addition, the unprecedented sensitivity of ALMA has made possible the detection of a wealth of weak lines ensuring a more accurate characterization of the chemistry associated with the cores.

To date, the chemical inventory of only a handful of sources has been extensively studied with interferometers. These include the low-mass protobinary system IRAS 16293–2422 (hereafter IRAS 16293, Jørgensen et al., 2016) and the high-mass star-forming regions associated with Sgr B2(N) (Belloche et al., 2016) and Orion KL (Pagani et al., 2017). Therefore, there is a substantial need for the continued investigation of additional hot cores in order to build up a database of the molecular inventories and temperatures characterising these sources. Such a database will provide the statistics needed for new insights into the physical and chemical processes at play during the formation of hot cores

and will help the classification of sources according to evolutionary stage.

To this end, the high-mass hot core of AFGL 4176 has been investigated with ALMA and for the first time, a comprehensive study of the chemical inventory of the source is presented. The results of this work are compared with other high- and low-mass sources, in addition to the predictions of hot core chemical models.

4.1.1 AFGL 4176

AFGL 4176, located in the southern hemisphere at $13^{\text{h}}43^{\text{m}}01.704^{\text{s}}$, $-62^{\circ}08'51''23$ (ICRS J2000), was first identified by Henning et al. (1984) through its bright infrared spectrum as a young and massive star embedded in a thick dusty envelope. The source has been further characterised by Beltrán et al. (2006), who used large-scale millimetre continuum observations carried out with the Swedish-ESO Submillimetre Telescope (SEST), to identify a compact core of approximately $1120 M_{\odot}$ with a diameter of 1 pc and luminosity of $2 \times 10^5 L_{\odot}$ (assuming a distance of 5.3 kpc). It should be noted however, that the distance to AFGL 4176 is not well-constrained and cited values range from 3.5 to 5.3 kpc (see, Boley et al., 2012, and references therein), with the most frequently cited distance being 4.2 kpc, based on observations of CH_3OH masers (Green & McClure-Griffiths, 2011). However, in this work we will assume a distance of 3.7 kpc, based on the recent second release of *Gaia* data, which places the source at a distance of $3.7_{-1.6}^{+2.6}$ kpc (Bailer-Jones et al., 2018).

In addition to the large-scale envelope, strong evidence that the system contains a Keplerian-like disk is presented by Johnston et al. (2015) who use observations of CH_3CN obtained with ALMA to trace the disk kinematics on scales of ~ 1200 au. A disk-like structure is consistent with the models reported by Boley et al. (2012) who combine interferometric and photometric observations of AFGL 4176 and use radiative transfer and geometric models to characterise the source. Although the observations are generally well described by one-dimensional models, Boley et al. (2012) find substantial deviations from spherical symmetry at scales of tens to hundreds of astronomical units. On these scales, the observations are better described by a multi-component model consisting of a Gaussian halo and an inclined circumstellar disk. Knots of shocked H_2 emission have also been identified around AFGL 4176, potentially indicating an outflow, though no preferred spatial direction was revealed (De Buizer, 2003).

A limited number of detections of molecular species have been reported towards AFGL 4176. CO_2 and H_2O have been identified in observations carried out with the *Infrared Space Observatory* (van Dishoeck et al., 1996; van Dishoeck & Helmich, 1996; Boonman et al., 2003) and detections of CO , NH_3 and CH_3CN by the Atacama Pathfinder Experiment (APEX) and ALMA have been reported by Johnston et al. (2014, 2015). In addition, a number of CH_3OH masers are reported in the vicinity of the source (Phillips et al., 1998; Green & McClure-Griffiths, 2011). However, so far no reports of a more comprehensive chemical inventory of the source exist.

This paper presents an extensive study of the molecular species detected towards AFGL 4176, in addition to those previously reported. The work is based on the same set of high sensitivity, high resolution ALMA observations as analysed by Johnston et al. (2015), but focuses on identifying and characterising all molecular species with transitions in the observed frequency range associated with the source, rather than the disk kinematics. The high sensitivity of ALMA makes it possible to identify weak and optically thin lines while the unique spatial resolving power ensures that the analysed emission stems from the disk around the central forming star rather than the large-scale surrounding envelope.

The structure of the paper is as follows: Sect. 4.2 introduces the observations, calibration process and methods used for identifying molecular species. Section 4.3 lists all detected species, our derived molecular column densities and excitation temperatures and discusses the spatial distribution of selected molecules. Section 4.4 compares the results for AFGL 4176 with observations of other objects and with model predictions. Finally, Sect. 4.5 summaries the results and conclusions.

4.2 Observations and methods

4.2.1 Observations

Observations of AFGL 4176 were carried out with ALMA during Cycle 1 (program 2012.1.00469.S, see Johnston et al., 2015, for first results) with 39 antennas in the array, between August 16, 2014 and August 17, 2014 using the Band 6 receivers, covering the frequency range of 211 – 275 GHz. Four spectral windows were obtained covering a total bandwidth of ~ 4.7 GHz. These consist of two wide windows, of 1875 MHz, centred at 240.5 and 254.0 GHz and two narrow windows, of 468.75 MHz, centred at 239.0 and 256.3 GHz. The spectral resolution of the observations is 976.6 kHz (~ 1.2 km s $^{-1}$) and 244 kHz (~ 0.3 km s $^{-1}$) for the wide and narrow windows, respectively. The angular resolution is $\sim 0.35''$, equivalent to ~ 1285 au at the distance of AFGL 4176.

The data were downloaded from the ALMA archive and reduced via the delivered pipeline script using the Common Astronomy Software Applications (CASA) version 4.2.1. Bandpass and absolute flux calibration was carried out, respectively, using J1617-5848 and Titan, on August 16 and J1427-4206 and Ceres on August 17. The phase and gain calibration was carried out, respectively, using J1308-6707 and J1329-5608 on both days. The uncertainty on the flux calibration is estimated to be $\leq 20\%$. The data were continuum subtracted using the most line-free channels and corrected for primary beam attenuation.

The continuum and line data were imaged separately in CASA version 5.1.1-5 using a pixel size of $0.04''$, a velocity resolution for the spectral cubes of 1.2 km s $^{-1}$ and Briggs weighting with a robust parameter of 1.5. The peak continuum emission is 29 mJy beam $^{-1}$ (5.7 K at 247 GHz) with an rms noise of approximately 0.5 mJy beam $^{-1}$ (0.1 K at 247 GHz) in a beam of $0''.33 \times 0''.31$. The coordinates of the continuum peak were determined by 2D Gaussian fitting in the image plane to be $13^{\text{h}}43^{\text{m}}01.699^{\text{s}}$, $-62^{\circ}08'51''.249$ (IRCS J2000). Table 4.1 lists the frequencies covered and the rms noise per 1.2 km s $^{-1}$ channel derived for each of the spectral windows.

For each of the imaged cubes, a spectrum is extracted at the location of the peak continuum emission. Each spectrum represents the average over an area equivalent to the size of the synthesised beam ($\sim 0''.3$). Figure 4.1 shows the continuum and the location at which the spectra were extracted. In addition to the main continuum peak, labelled mm1 by Johnston et al. (2015), a secondary peak is observed $\sim 1''$ north-west of the primary peak; this peak is labelled mm2. A counterpart to this secondary peak is observed to the south-east of mm1 (outside the plotted region). These two peaks are located perpendicular to the major axis of mm1 and may indicate a large-scale outflow, consistent with the CO observations presented by Johnston et al. (2015). For this work however, the focus is on the main continuum peak and all subsequent discussion refers to this source only.

Table 4.1: Overview of spectral cubes

Frequency [GHz]	Beam [" × " (P.A.°)]	rms noise	
		[mJy beam ⁻¹]	[K]
238.838 – 239.306	0''35 × 0''29 (-31.6)	1.9	0.40
239.604 – 241.478	0''34 × 0''30 (-31.2)	1.5	0.31
253.107 – 254.980	0''33 × 0''28 (-30.8)	1.7	0.35
256.115 – 256.583	0''32 × 0''28 (-32.3)	2.2	0.46

Notes. The listed rms noise is determined over the line-free channels. The channel width is 1.2 km s⁻¹.

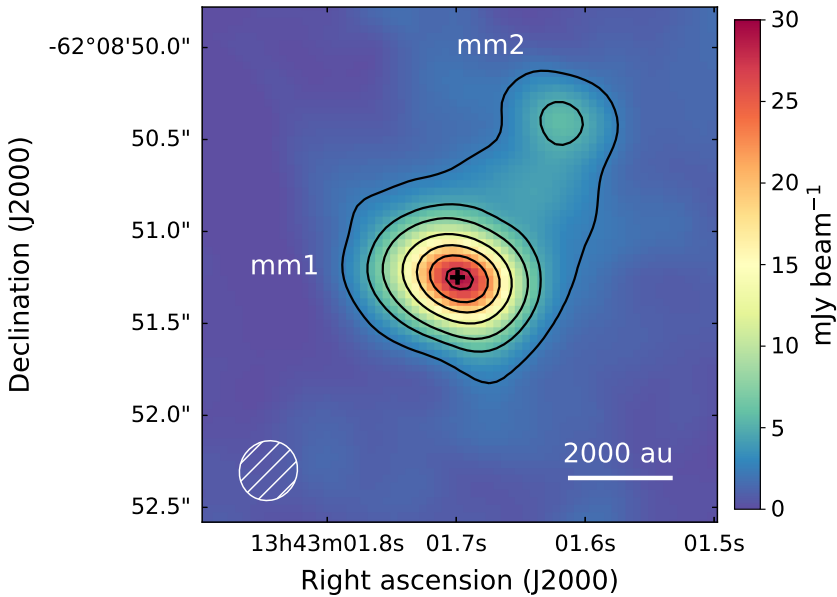


Figure 4.1: Continuum image of AFGL 4176 at 1.2 mm. Contours are [5, 10, 15, 25, 35, 45, 55] σ , with $\sigma = 0.5$ mJy beam⁻¹. The peak continuum location at which the spectra have been extracted is marked by the black cross. The synthesised beam ($0''33 \times 0''31 \sim 1210 \times 1140$ au) is shown in the bottom left corner.

4.2.2 Methods for line identification and modelling

For the identification of spectral lines, catalogued transition frequencies from the JPL (Jet Propulsion Laboratory¹, Pickett et al., 1998) and CDMS (Cologne Database for Molecular Spectroscopy², Müller et al., 2001, 2005) molecular databases are compared with the extracted spectra. Observed lines are considered detected if the peak signal-to-noise ratio is three or higher. Species with fewer than five detected lines are considered tentative detections. Using the CASSIS³ line analysis software and assuming local thermodynamic equilibrium (LTE) and optically thin lines, a synthetic spectrum is produced for each identified species. This is done by providing CASSIS with the following parameters: excitation temperature, T_{ex} [K], column density of the species, N_{s} [cm⁻²], source velocity, v_{LSR} [km s⁻¹], line width at half maximum [km s⁻¹], and angular size of the emitting region (assumed to be equal to the area of the synthesised beam), θ_{s} ['].

For two species, CH₃CN and HC₃N, vibrationally excited transitions are detected (see Sect. 4.3). For vibrationally excited CH₃CN the JPL database is used. This entry utilises a partition function in which vibrational contributions are taken into account. In contrast, the CDMS entries for vibrationally excited HC₃N, and isotopologues hereof, do not include vibrational contributions but list these separately. Therefore, vibrational correction factors of 1.17 and 1.48 for the main and ¹³C-isotopologues of HC₃N, respectively, have been applied to all listed values.

Excitation temperatures and column densities are determined for species which have three or more unblended lines detected, that is lines with a signal-to-noise ratio of three or higher, whose emission can mainly be attributed to one molecule, and these span upper state energies of at least 100 K. This is done by creating grids of models varying T_{ex} and N_{s} and identifying the model with the minimal χ^2 as the best fit. The models are optimised to fit all unblended lines detected for each species. Table A.1 lists the model grids for each of the fitted species. The uncertainty on T_{ex} and N_{s} is listed as the standard deviation of models within the 95% confidence level. For most species these are about 20%, though for CH₃CHO and (CH₂OH)₂ the uncertainty on T_{ex} is up to 85%. The uncertainty on column density ratios with respect to methanol is calculated through the propagation of errors. For species where less than three unblended lines are detected, or species where upper state energies of the detected lines do not span more than 100 K, the column density is derived assuming a fixed excitation temperature. In the case of CH₃OH and the isotopologues of SO₂, the excitation temperature is assumed to be 120 K and 150 K, based on the ¹³C-methanol isotopologue and main isotopologue of SO₂, respectively. For all other species, the excitation temperature is assumed to be 200 K. This value is the average of the best-fit excitation temperatures derived for the 12 species listed at the top of Table 4.2. However, since the spread in best-fit excitation temperatures is fairly large, standard deviation of ~ 70 K, column densities are also derived assuming excitation temperatures of 130 K and 270 K. For all species but CH₃COCH₃, the column densities derived at these temperatures are within 50% of the value derived assuming $T_{\text{ex}} = 200$ K. For CH₃COCH₃, column densities at 130 K and 270 K are within a factor of three of the value derived assuming $T_{\text{ex}} = 200$ K.

To ensure that no lines are incorrectly assigned, three checks are conducted. First, that the best-fit model for each species does not predict lines at frequencies, covered by the observations, where no emission is detected. Second, that no other species, for which

¹<http://spec.jpl.nasa.gov>

²<http://www.ph1.uni-koeln.de/cdms/>

³Centre d'Analyse Scientifique de Spectres Instrumentaux et Synthétiques;
<http://cassis.irap.omp.eu>

the spectroscopy is known and listed in either of the databases mentioned above, can reproduce the line without predicting lines at frequencies where no emission is detected. Finally, that isotopically rare species do not predict lines of the main isotopologue where no emission is detected.

The excitation temperatures and column densities for $^{13}\text{CH}_3\text{OH}$ and CH_3CN are derived first because their lines are very numerous, bright and span a large range of upper state energies. Based on fits to these species, a source velocity of -53.5 km s^{-1} and FWHM line widths of 6 km s^{-1} are found. These values are kept fixed for the subsequent fitting of other species.

Finally, in order to compare the derived molecular column densities across different objects, CH_3OH is used as a reference. Methanol is used as a reference because it is usually one of the most abundant species in hot cores and is thought to be the parent molecule for most complex organics. However, because this species is very abundant, many of its lines are optically thick and therefore its column density cannot be derived directly. The column density of CH_3OH is instead estimated based on the best-fit value for its ^{13}C -isotopologue, adopting a $^{12}\text{C}/^{13}\text{C}$ values of 60, derived assuming a galactocentric distance (d_{GC}) of 6.64 kpc and the relation for $^{12}\text{C}/^{13}\text{C}$ reported by Milam et al. (2005).

4.3 Results

A total of 354 lines are identified towards AFGL 4176 with a signal-to-noise ratio of three or above. Of these, 324 lines can be assigned to a total of 23 different molecular species or their isotopologues. Fifteen species have five or more detected transitions while eight species have fewer than five detected transitions and are therefore considered tentative detections. For the remaining 30 lines no match to known transitions was found. A list of frequencies and peak intensities for these unidentified lines is given in Appendix B. With a total covered bandwidth of $\sim 4.7 \text{ GHz}$, the line density is roughly 75 lines per GHz or one line per 13.3 MHz (ALMA Band 6). For comparison, the ALMA-PILS survey towards the low-mass protobinary system IRAS 16293 found one line per 3.4 MHz (ALMA Band 7, Jørgensen et al., 2016). This high density means that detected lines are often blended with emission from other species. Therefore, as noted above, great caution is exercised when lines are assigned to species.

Table 4.2 list all identified species, isotopologues and isomers. The Table also summarises the number of identified lines, both unblended and blended, the range of upper state energies and Einstein A coefficients covered by these lines as well as the derived excitation temperature and column density for each species. It should be noted that hyperfine transitions with the same catalogued frequency are counted as a single line since these are indistinguishable in the data. After the identification and modelling of individual species the synthetic spectra are summed to obtain a full model for AFGL 4176. Figure 4.2 shows the full model for the spectral window centred at 239.1 GHz (see Appendix C for full model of other spectral windows).

The derived excitation temperatures range between 120 and 320 K with an average of 200 K, consistent with the range of temperatures derived for CH_3CN by Johnston et al. (2015). The highest column density is $5.5 \times 10^{18} \text{ cm}^{-2}$, derived for CH_3OH (based on $^{13}\text{CH}_3\text{OH}$ and corrected with the $^{12}\text{C}/^{13}\text{C}$ ratio), while the lowest values is $1.8 \times 10^{14} \text{ cm}^{-2}$, derived for HC^{15}N . While these column densities span more than four orders of magnitude, the majority of species have column densities between 10^{16} and 10^{17} cm^{-2} . The species with the highest number of detected lines, 41 in total, is CH_3OH .

Table 4.2: Summary of detected lines and derived values of N_s and T_{ex}

Species	Name	N_{lines}		E_{up} [K]	A_{ij} $\times 10^{-5} [\text{s}^{-1}]$	Catalogue	N_s [cm^{-2}]	T_{ex} [K]	X/CH ₃ OH [%]
		Unblended	Blended						
¹³ CH ₃ OH	Methanol	7	5	60 – 644	2.31 – 8.81	CDMS	$(9.2 \pm 0.6) \times 10^{16}$	120 ± 15	1.67 ± 0.16
CH ₃ C ₂ H	Propyne	9	1	86 – 346	3.85 – 5.83	CDMS	$(3.8 \pm 0.7) \times 10^{16}$	320 ± 90	0.69 ± 0.14
CH ₃ CN	Methyl cyanide (Acetonitrile)	9	0	80 – 537	73 – 118	JPL	$(3.4 \pm 0.3) \times 10^{16}$	270 ± 40	0.62 ± 0.07
CH ₃ CN, $v_8=1$		14	2	600 – 955	94 – 111	JPL	$(4.3 \pm 0.6) \times 10^{16}$	220 ± 40	0.78 ± 0.12
CH ₃ CHO	Acetaldehyde	4	4	93 – 490	3.85 – 56.3	JPL	$(1.5 \pm 0.8) \times 10^{16}$	160 ± 125	0.27 ± 0.15
NH ₂ CHO	Formamide	10	3	68 – 439	2.48 – 115	CDMS	$(1.0 \pm 0.09) \times 10^{16}$	190 ± 35	0.18 ± 0.02
H ₂ CS		7	1	46 – 519	5.43 – 20.5	CDMS	$(4.3 \pm 0.2) \times 10^{16}$	160 ± 10	0.78 ± 0.07
CH ₃ OCH ₃	Methyl ether	17	5	26 – 502	2.40 – 8.72	CDMS	$(1.3 \pm 0.1) \times 10^{17}$	160 ± 15	2.36 ± 0.25
C ₂ H ₅ OH	Ethanol	7	4	11 – 35 – 450	1.93 – 41	JPL	$(8.7 \pm 1.2) \times 10^{16}$	120 ± 25	1.58 ± 0.25
C ₂ H ₃ CN	Vinylcyanide	8	4	153 – 388	114 – 136	CDMS	$(6.2 \pm 1.1) \times 10^{15}$	240 ± 105	0.11 ± 0.02
CH ₃ OCHO	Methyl formate	14	5	101 – 473	0.66 – 24.8	JPL	$(1.7 \pm 0.3) \times 10^{17}$	310 ± 75	3.09 ± 0.59
<i>aGg</i> (CH ₂ OH) ₂	Ethylene glycol	14	16	30 – 144 – 327	3.76 – 40.9	CDMS	$(3.0 \pm 0.5) \times 10^{16}$	160 ± 130	0.55 ± 0.10
<i>gGg</i> (CH ₂ OH) ₂		12	8	62 – 229	2.93 – 14.3	CDMS	$(2.6 \pm 0.6) \times 10^{16}$	140 ± 120	0.47 ± 0.11
SO ₂	Sulphur dioxide	6	0	36 – 333	2.67 – 13.3	JPL	$(8.1 \pm 1.9) \times 10^{17}$	150 ± 30	14.7 ± 3.6
CH ₃ OH		31	10	20 – 950	1.56 – 8.80	JPL	$(5.5 \pm 0.4) \times 10^{18}$ ^(a)	[120]	≡100
H ₂ CCO	Ketene	1	0	88	15.5	CDMS	$(9.2 \pm 1.5) \times 10^{15}$	[200]	0.17 ± 0.03
HNCO	Isocyanic acid	1	0	113	19.0	CDMS	$(6.2 \pm 1.3) \times 10^{16}$	[200]	1.13 ± 0.25
NS	Nitrogen sulphide	4	2	39	0.93 – 28.4	JPL	$(1.2 \pm 0.1) \times 10^{16}$	[200]	0.22 ± 0.02
C ⁶⁴ S	Carbon sulphide	1	0	35	28.6	JPL	$(8.1 \pm 1.6) \times 10^{15}$	[200]	0.15 ± 0.03
t-HCOOH	Formic acid	1	1	70	15.7	CDMS	$(4.3 \pm 0.6) \times 10^{16}$	[200]	0.78 ± 0.12
SO	Sulphur monoxide	1	0	100	0.43	JPL	$(7.0 \pm 1.5) \times 10^{17}$	[200]	12.7 ± 2.9
³⁴ SO		1	0	56	20.4	JPL	$(1.8 \pm 0.5) \times 10^{16}$	[200]	0.33 ± 0.1
HC ₃ N, $v=0$	Cyanoacetylene	1	0	177	132	CDMS	$(6.2 \pm 2.2) \times 10^{15}$	[200]	0.11 ± 0.04
HC ₃ N, $v_7=2$		1	2	820 – 823	132 – 133	CDMS	$(2.5 \pm 0.6) \times 10^{16b}$	[200]	0.45 ± 0.11
HCC ¹³ CN		1	0	177	130	CDMS	$(3.8 \pm 0.8) \times 10^{14}$	[200]	0.007 ± 0.002
HCCC ¹⁵ N		1	0	184	134	CDMS	$(1.8 \pm 0.4) \times 10^{14}$	[200]	0.003 ± 0.001
HCC ¹³ CN, $v_7=1$		2	0	495 – 496	130 – 131	CDMS	$(8.1 \pm 1.2) \times 10^{14c}$	[200]	0.01 ± 0.002
C ₂ H ₅ CN	Ethyl cyanide (Propionitrile)	9	4	79 – 189	6.22 – 142	CDMS	$(6.4 \pm 0.8) \times 10^{15d}$	[200]	0.12 ± 0.02
CH ₃ COCH ₃	Acetone	13	2	74 – 235	2.43 – 659	JPL	$(5.3 \pm 0.5) \times 10^{16d}$	[200]	0.96 ± 0.11
CH ₂ (OH)CHO	Glycolaldehyde	2	1	111 – 143	12.0 – 27.9	CDMS	$\leq 1.1 \times 10^{16e}$	[200]	≤0.2
O ¹³ CS	Carbonyl sulphide	1	0	134	4.80	CDMS	$(5.5 \pm 0.7) \times 10^{15}$	[200]	0.10 ± 0.01
³³ SO ₂		10	8	72 – 471	0.13 – 19.6	JPL	$(1.3 \pm 0.8) \times 10^{16d}$	[150]	0.24 ± 0.15
³⁴ SO ₂		1	1	82 – 182	2.66 – 12.8	JPL	$(8.1 \pm 1.8) \times 10^{16}$	[150]	1.47 ± 0.34
SO ¹⁸ O		1	2	69 – 89	0.11 – 18.3	JPL	$(7.6 \pm 1.0) \times 10^{15}$	[150]	0.14 ± 0.02

Notes. Values in square brackets are fixed. (a) Based on ¹³C/CH₃OH, assuming a ¹²C/¹³C ratio of 60. (b) Includes the vibrational correction factor of 1.17. (c) Includes the vibrational correction factor of 1.48. (d) Column density derived assuming fixed T_{ex} due to insufficient range of E_{up} of unblended lines. (e) Upper limit due to low signal-to-noise.

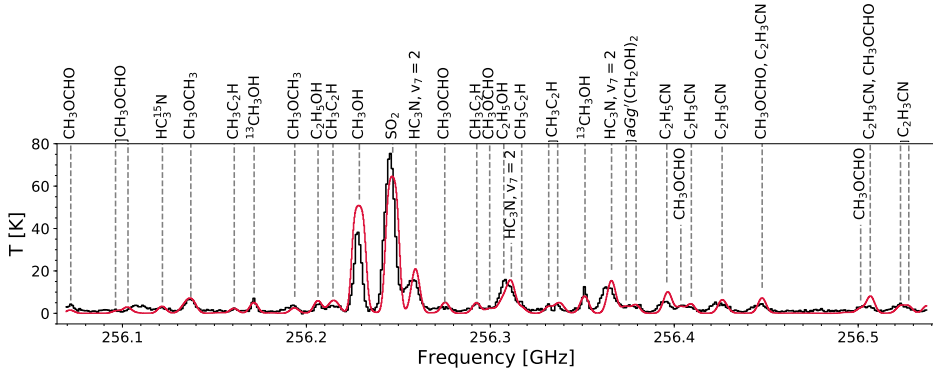


Figure 4.2: Full model (red), i.e., the sum of synthetic spectra, for all species detected towards AFGL 4176 in the spectral window centred at 256.3 GHz. Frequencies are shifted to the rest velocity of the region. The data are shown in black.

These lines also span the largest range of upper state energies ranging from 20 to 950 K. Similarly, the range of upper state energies of the ^{13}C -isotopologue of methanol span 60 to 640 K, though only twelve lines associated with this isotopologue are detected. For the remaining species, the number of detected lines range from a single line up to 30 lines in the case of $aGg'(\text{CH}_2\text{OH})_2$, though it should be noted that more than half of these are blended with emission from other species. On average the upper state energies of species span a range of 300 K.

By far the highest column density ratios with respect to methanol are derived for SO_2 and SO with values of 14.7% and 12.7%, respectively. The remaining species have column density ratios with respect to methanol ranging between 0.003% and 3%, with most species showing ratios of the order of 0.1%. On average, the column density ratios derived for O-bearing species are a factor of three higher than those derived for N-bearing species. This trend will be further discussed in sect. 4.4.

Vibrationally excited transitions are detected for two species, CH_3CN and HC_3N . In both cases, the column density ratio derived from the vibrationally excited transitions are higher than those derived for the ground-state vibrational transitions; 0.78% vs 0.62% for $\text{CH}_3\text{CN}/\text{CH}_3\text{OH}$ and 0.45% vs 0.11% for $\text{HC}_3\text{N}/\text{CH}_3\text{OH}$. Note that for the latter species only one and three lines are detected for the ground and vibrationally excited states respectively. That the column densities derived based on the vibrationally excited states are higher than those derived from the ground-state vibrational transitions is most likely not representative of the actual distribution of molecules but rather due to the fact that the vibrationally excited transitions are excited via shocks or infrared pumping and therefore not in LTE. The column densities derived from these transitions can therefore not be trusted.

4.3.1 Upper limit on the column density of glycolaldehyde

A number of transitions of glycolaldehyde are covered by the data although only three of these lines, one of which is blended, are considered detected. These lines have signal-to-noise ratios of approximately four. The remaining lines identified as likely to be due to

Table 4.3: Summary of isotopologues with only blended lines

Species	N _{lines}			E _{up} [K]	A _{ij} ×10 ⁻⁵ [s ⁻¹]	Catalogue	N _s [cm ⁻²]	T _{ex} [K]
	Unblended	Blended	Total					
CH ₃ ¹³ CN	0	6	6	80 – 259	100 – 118	JPL	[5.7×10 ¹⁴] ^a	[270]
HC ¹³ CCN	0	1	1	177	130	CDMS	[3.8×10 ¹⁴]	[200]
H ¹³ CCCN, v ₇ =1	0	2	2	479 – 503	108 – 133	CDMS	[8.1×10 ¹⁴]	[200]
HC ¹³ CCN, v ₇ =1	0	2	2	493	130 – 131	CDMS	[8.1×10 ¹⁴]	[200]

Notes. Values in square brackets are fixed. ^(a) Based on CH₃CN, assuming a ¹²C/¹³C ratio of 60.

glycolaldehyde, five in total, are detected with signal-to-noise ratios of between two and three and are therefore not included in the line list in Table 2.2. Due to the generally low signal-to-noise of the glycolaldehyde lines, we report an upper limit column density for this species. The upper limit is derived based on the two unblended lines and assumes an excitation temperature of 200 K. The column density upper limit is $\leq 1.1 \times 10^{16}$ cm⁻², equivalent to $\leq 0.2\%$ with respect to methanol.

The formation pathway of glycolaldehyde has recently been investigated in the laboratory by Chuang et al. (2017). They find that the relative abundance of this and other complex species, can be used as a diagnostic tool to derive the processing history of the ice in which the species formed. In particular, the ratio of glycolaldehyde to ethylene glycol provides a good handle on distinguishing ices processed purely by atom-addition (hydrogenation), ices processed purely by UV irradiation or ice processed by both. In the case of AFGL 4176, the ratio of glycolaldehyde to ethylene glycol is ≤ 0.4 . This ratio is consistent with relative abundances of the species formed in experiments where ice analogues are exposed to both UV irradiation and hydrogenation.

4.3.2 Isotopologues with only blended lines

Three isotopologues of HC₃N and one of CH₃CN are detected towards AFGL 4176, although only through blended lines. For completeness, these isotopologues are included in the full model. Since no column density and excitation temperature can be derived from the blended lines these are adopted from the isotopologues for which unblended lines are detected. That is, for HC¹³CCN the column density derived for HCC¹³CN is adopted, while for vibrationally excited H¹³CCCN and HC¹³CCN the column density derived for vibrationally excited HCC¹³CN is adopted. In the case of CH₃¹³CN, the column density derived for the main isotopologue has been corrected by the ¹²C/¹³C ratio of 60. The isotopologues and the adopted column densities and excitation temperatures are listed in Table 4.3. It should be noted that no lines of either H¹³CCCN, ¹³CH₃CN or CH₃C¹⁵N, were covered by the data. A couple of transitions of vibrationally excited CH₃¹³CN are within the data range but since these are all weak and highly blended they could not be modelled.

4.3.3 Spatial distribution of selected species

Two line maps are produced for each of the species for which five or more unblended lines are detected. The imaged lines are chosen so that both high and low upper state energy transitions are represented, in order to investigate whether these occupy different

spatial regions. Also, only lines which are relatively isolated, that is to say whose peak frequency is separated by at least 3 km s^{-1} from neighbouring peaks, are imaged. This is done in order to minimise line confusion. After suitable lines have been identified for each species, the zero- and first-moment maps, that is the velocity integrated intensity map and intensity-weighted velocity map, respectively, are produced. The spatial extent of each species is determined by fitting a 2D Gaussian to the zero-moment maps. As a representative sample of these maps, the lines of CH_3OH , NH_2CHO and $\text{CH}_3\text{C}_2\text{H}$ are shown in Fig. 4.3; maps for the remaining species are presented in Appendix D.

There are no large differences between the spatial distribution of O- and N-bearing species. Except for $\text{CH}_3\text{C}_2\text{H}$, all species have emission peaks near the position of the continuum peak. The N-bearing species (CH_3CN , $\text{C}_2\text{H}_3\text{CN}$ and $\text{C}_2\text{H}_5\text{CN}$) peak very close to the continuum peak, while some O-bearing species (CH_3OH and CH_3OCH_3 e.g.) peak up to $0''.2$ away from the continuum peak. Although this scale is of the same order as the size of the synthesised beam, the signal-to-noise of these maps (30 – 90) is large enough to make these spatial differences significant.

Noticeable differences in spatial distributions exist between transitions of the same species with low and high upper state energies. For SO_2 , H_2CS , CH_3CN , $\text{C}_2\text{H}_5\text{OH}$ and CH_3OCHO low E_{up} transitions are more extended ($\sim 0''.7$) than high E_{up} transitions ($\sim 0''.55$). The larger spatial extent of low E_{up} transitions indicates that these species are present in colder gas. This is consistent with the relatively low excitation temperatures derived for SO_2 , H_2CS and $\text{C}_2\text{H}_5\text{OH}$, 150 K, 160 K and 120 K, respectively, but contradicts the high excitation temperatures derived for CH_3CN and CH_3OCHO , 270 K and 310 K, respectively. For $\text{C}_2\text{H}_3\text{CN}$ and $\text{C}_2\text{H}_5\text{CN}$ this trend is reversed, with the spatial extent of low E_{up} transitions smaller ($\sim 0''.4$) than that of high E_{up} transitions ($\sim 0''.55$). For the remaining species (CH_3OH , NH_2CHO , CH_3OCH_3 and CH_3COCH_3) the extent of low and high E_{up} transitions are similar.

Finally, as noted above, $\text{CH}_3\text{C}_2\text{H}$ is the only species whose emission is not concentrated at the location of the continuum peak emission. Instead this species shows two peaks, of approximately similar intensity, with one roughly coinciding with that of the continuum and a second at the location of the secondary continuum peak, mm2. The spatially more diffuse emission of this species is consistent with trends observed towards other hot cores (see e.g. Fayolle et al., 2015).

For a number of species a velocity gradient is detected across the source. The gradient is most pronounced in the case of NH_2CHO but also visible in the high upper state energy lines of CH_3CN , CH_3OCHO , $\text{C}_2\text{H}_3\text{CN}$ and $\text{C}_2\text{H}_5\text{CN}$. The presence of a velocity gradient across the sources is consistent with the result of Johnston et al. (2015) who model the emission of CH_3CN and find this to be consistent with a Keplerian-like disk.

4.4 Discussion

Table 4.4 presents an overview of all detected O-, N- and S-bearing species (isotopologues not included) towards AFGL 4176. These detected species are common in regions of star-formation (see review by Herbst & van Dishoeck, 2009, and references therein), although a few rarer isotopologues such as C^{34}S and ^{18}O -, ^{34}S - and ^{33}S -sulphur dioxide are also detected.

On average, the column density ratios with respect to methanol derived for the O-bearing species are a factor of three higher than the ratios derived for the N-bearing species. Also, the excitation temperatures derived for the O-bearing species are generally low, 120 – 160 K, while the excitation temperatures derived for the N-bearing species are

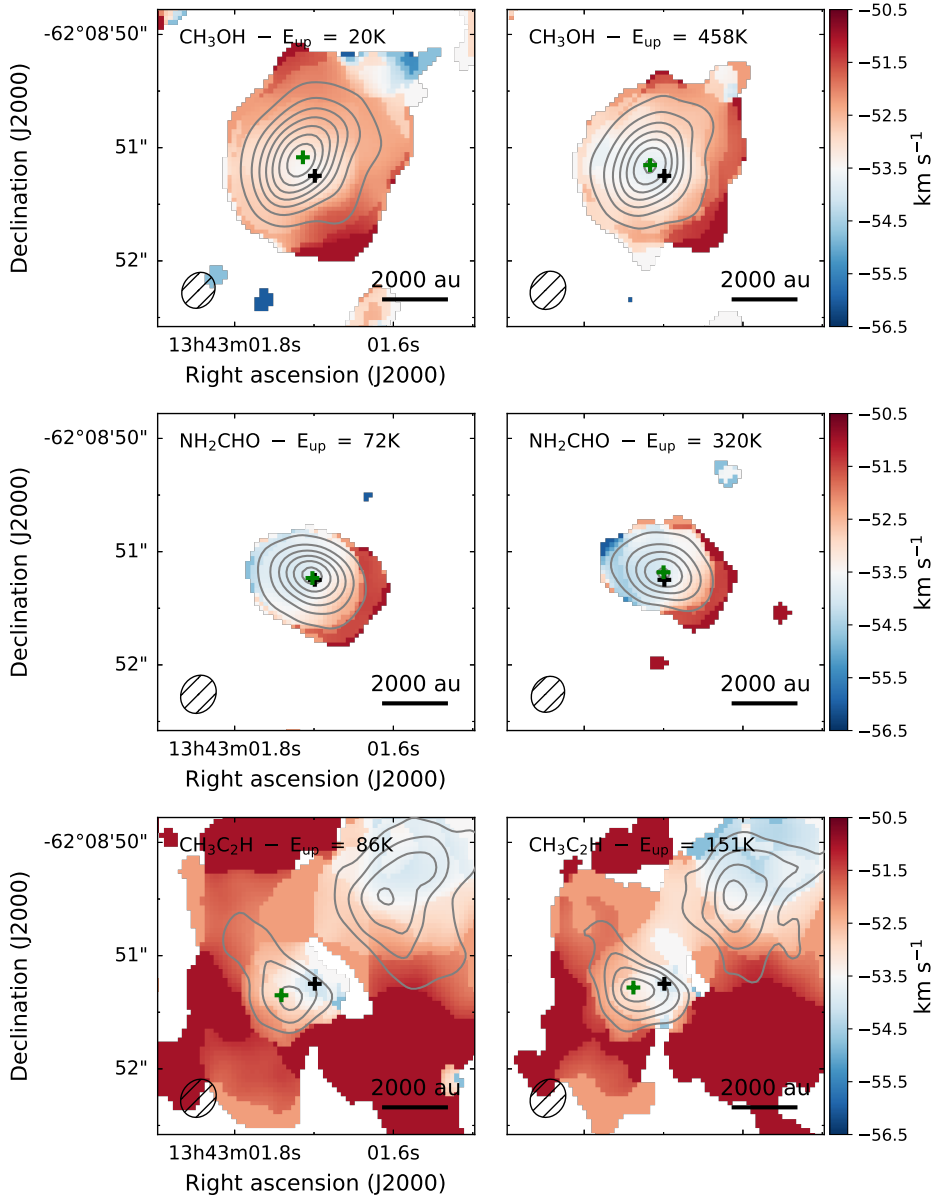


Figure 4.3: *Top panels:* First-moment (intensity-weighted velocity) map of CH_3OH lines at 254.0153 GHz (left) and 241.2679 GHz (right). Pixels with signal-to-noise ratios of less than three are masked out. The zero-moment (integrated intensity) map for each line is overlaid in grey contours. Contours start at 9σ and are in steps of 12σ , with $\sigma = 1.34 \times 10^{-2}$ and 7.16×10^{-3} $\text{Jy beam}^{-1} \text{ km s}^{-1}$, for the left and right panel, respectively. The black and green crosses mark the locations of the peak continuum emission and peak integrated line intensity, respectively. *Middle panels:* Same as top panels but for NH_2CHO lines at 239.952 GHz (left) and 254.727 GHz (right). Contours start at 9σ and are in steps of 12σ , with $\sigma = 6.17 \times 10^{-3}$ and 6.25×10^{-3} $\text{Jy beam}^{-1} \text{ km s}^{-1}$, for the left and right panel, respectively. *Bottom panels:* Same as top panels but for $\text{CH}_3\text{C}_2\text{H}$ lines at 239.2523 GHz (left) and 239.2112 GHz (right). Contours start at 6σ and are in steps of 3σ , with $\sigma = 7.29 \times 10^{-3}$ and 6.35×10^{-3} $\text{Jy beam}^{-1} \text{ km s}^{-1}$, for the left and right panel, respectively.

Table 4.4: Overview of oxygen-, nitrogen and sulphur-bearing species detected towards AFGL 4176

O-bearing	N-bearing	S-bearing
CH ₃ OH	CH ₃ CN	H ₂ CS
CH ₃ CHO	C ₂ H ₃ CN	O, N-bearing
C ₂ H ₅ OH	C ₂ H ₅ CN	NH ₂ CHO
CH ₃ OCH ₃	HC ₃ N	HNCO
CH ₃ COCH ₃	Hydrocarbons	O, S-bearing
CH ₃ OCHO	CH ₃ C ₂ H	SO ₂
(CH ₂ OH) ₂		SO
H ₂ CCO		N, S-bearing
t-HCOOH		NS
CH ₂ (OH)CHO		

Notes. Not including isotopologues. Species in red have fewer than five detected transitions and are considered tentative.

generally high, 190 – 240 K. This differentiation of species with excitation temperature is similar to trends observed in the Orion molecular cloud (Blake et al., 1987; Crockett et al., 2015) and in the high-mass star-forming complex G19.62-0.23 (Qin et al., 2010). Similar trends are also reported by Suzuki et al. (2018) who carry out a survey of N- and O-bearing species towards eight high-mass star forming regions, including Orion KL and G19.62-0.23, using the 45m radio telescope at the Nobeyama Radio Observatory. When comparing these observations with chemical models, Suzuki et al. (2018) conclude that the correlations between fractional abundances of different groups of species can be explained by a combination of different temperature structures inside the cores and different evolutionary phases of the studied regions. As examples of a younger, less evolved source and an older, more evolved source, Suzuki et al. (2018) discuss NGC 6334F (also known as NGC 6334I) and G10.47+0.03, respectively. While G10.47+0.03 displays a relatively high fractional abundance of N-bearing species, $\sim 2 - 10\%$ with respect to methanol, the fractional abundances of the same species detected towards NGC 6334F are only $\sim 0.1\%$. By assuming a more dominant high-temperature region (~ 200 K) and later evolutionary stage for G10.47+0.03 with respect to NGC 6334F, Suzuki et al. (2018) reproduce the observed trends. The trend of younger regions being characterised by lower abundances of N-bearing species with respect to O-bearing species may be a consequence of gas-phase nitrogen chemistry taking longer to initiate compared with the chemistry of O-bearing species (Charnley et al., 1992).

The studies discussed above are primarily based on single-dish observations and therefore, mostly, spatially unresolved. This can be problematic when studying sites of star-formation, especially at large distances, since the emission associated with the inner hot envelope around the centrally forming star may not be distinguished from the emission of its cooler envelope. Also, since single-dish telescopes are generally less sensitive when compared with interferometric observations and especially ALMA, it may not be possible to identify enough optically thin lines from which excitation conditions can be derived. The generally larger beam sizes of single-dish telescopes may also result in underesti-

mated column densities of molecular species if effects of beam dilution are not accounted for correctly.

In the following, we compare our ALMA results for AFGL 4176 with a selection of ALMA studies, that suffer less from sensitivity and resolution limitations. These studies focus on the Galactic centre, Orion KL and the low-mass protostellar binary IRAS 16293. We conclude the section with a comparison to chemical models. Table 4.5 and Fig. 4.4 summarises the comparisons.

4.4.1 Comparison with the high-mass star-forming regions in Sgr B2(N) and Orion KL

Sgr B2(N): Located in the Galactic central region, the Sgr B2 molecular cloud hosts some of the most active sites of high-mass star-formation in the galaxy. One of these sites, Sgr B2 (N), is the subject of the ALMA line survey EMOCA (Exploring Molecular Complexity with ALMA, Belloche et al., 2016) aimed at characterising the molecular content of the region. Due to the high spatial resolution of the observations, $\sim 1.6''$, probing scales down to 0.06 pc (~ 13300 au assuming a distance of 8.34 kpc), Bonfand et al. (2017) were able to identify three new hot cores towards Sgr B2, labelled N3, N4 and N5, in addition to the previously identified cores N1 and N2. Bonfand et al. (2017) find that the chemical composition of these new cores are very similar to each other and very different from that of the N2 core, suggesting that the N2 core is chemically less evolved than the three new cores.

For the hot cores in Sgr B2, the column density ratio with respect to methanol of N-bearing species (CH_3CN , NH_2CHO , $\text{C}_2\text{H}_3\text{CN}$ and $\text{C}_2\text{H}_5\text{CN}$) are higher than those derived towards AFGL 4176 by up to two orders of magnitude. For the O-bearing species ($\text{C}_2\text{H}_5\text{OH}$ and CH_3OCHO), the variations are smaller, though still up to an order of magnitude higher in Sgr B2 compared with AFGL 4176.

In addition to the main isotopologues, a number of ^{13}C - and ^{15}N -isotopologues, as well as deuterated and vibrationally excited species, have been detected towards Sgr B2(N2) (Belloche et al., 2016). While no deuterated species are detected towards AFGL 4176, a number of lines of ^{13}C -cyanoacetylene are detected in addition to $^{13}\text{CH}_3\text{OH}$ and some blended lines of $\text{CH}_3^{13}\text{CN}$. ^{13}C doubly substituted cyanoacetylene isotopologues are also detected towards Sgr B2(N2). Towards AFGL 4176, two transitions of ^{13}C doubly substituted cyanoacetylene are covered but both are weak and highly blended. The tentative detection of HC_3^{15}N towards Sgr B2(N2) results in a ratio with respect to methanol identical to the value derived for AFGL 4176. It should be noted however, that only a very limited number of lines of these isotopologues are detected and therefore their detection is considered tentative and their ratios should be seen as indicative of trends rather than definite values.

Orion KL: Due to its proximity, ~ 388 pc from the Sun, the high-mass star-forming regions associated with the Orion molecular clouds are some of the most studied. Using ALMA observations, the morphology and molecular composition of the region was recently studied by Pagani et al. (2017) who, thanks to the high angular resolution of their data of $1.7''$, probing scales of ~ 660 au, were able to separate the region into a number of components and report a complex velocity structure. However, due to the lack of zero-spacing data to recover the extended emission of many species, Pagani et al. (2017) do not derive column densities or excitation temperatures for the detected species and limit their analysis to line identification and determination of line velocity and line widths. Orion KL may therefore be qualitatively compared with AFGL 4176 though no quantitative comparison is possible.

Table 4.5: Summary of column density ratios with respect to methanol predicted by models and derived towards AFGL 4176, Sgr B2(N) and IRAS 16293B

	X/CH ₃ OH [%]							
	Sgr B2		AFGL 4176	IRAS 16293B ^a	Model			
	(N2)	(N3-5)			Fast	Medium	Slow	
Hydrocarbons O-bearing	CH ₃ C ₂ H	–	–	0.69 ± 0.14	–	–	–	
	CH ₃ CHO	–	–	0.27 ± 0.15	1.20	0.03	0.10	0.37
	C ₂ H ₅ OH	5.0	7.6 – 10.4	1.58 ± 0.25	2.3	0.54	0.64	1.29
	CH ₃ OCH ₃	–	–	2.36 ± 0.25	2.4	0.44	0.69	0.74
	CH ₃ COCH ₃	–	–	0.96 ± 0.11	0.17	0.01	0.11	0.05
N-bearing	CH ₃ OCHO	3.0	18.9 – 32.0	3.09 ± 0.59	2.6	0.84	0.41	0.08
	(CH ₂ OH) ₂	–	–	(0.47 – 0.55) ± 0.1	0.5 – 0.55 ^b	0.03	0.01	10 ^{–4}
	CH ₃ CN	5.78	10.6 – 13.4	0.62 ± 0.07	0.4	0.04	0.02	0.03
	NH ₂ CHO	8.75	0.83 – 1.16 ^c	0.18 ± 0.02	0.1	3.55	1.65	0.08
	C ₂ H ₃ CN	1.05	0.6 – 1.25	0.11 ± 0.02	0.007	0.1	0.06	0.15
S-bearing	C ₂ H ₅ CN	17.25	4.8 – 8.11	0.12 ± 0.02	0.04	0.05	0.85	0.79
	NS	–	–	0.22 ± 0.02	–	–	–	–
	H ₂ CS	–	–	0.78 ± 0.07	0.02	–	–	–
	SO ₂	–	–	14.7 ± 3.6	0.02	0.67	0.84	2.05
	Reference	1, 2		this work	3, 4, 5, 6, 7, 8		9	

Notes. ^(a) Listed values are derived at 0.5'' (one beam) offset from IRAS 16293B. ^(b) Derived at 0.25'' (half beam) offset from IRAS 16293B. ^(c) Excluding the upper limit of ≤0.56% derived for N₄.

References. (1) Belloche et al. (2016); (2) Bonfand et al. (2017); (3) Coutens et al. (2016); (4) Jørgensen et al. (2016); (5) Lykke et al. (2017); (6) Calcutt et al. (2018); (7) Drozdovskaya et al. (2018); (8) Jørgensen et al. (2018); (9) Garrod (2013)

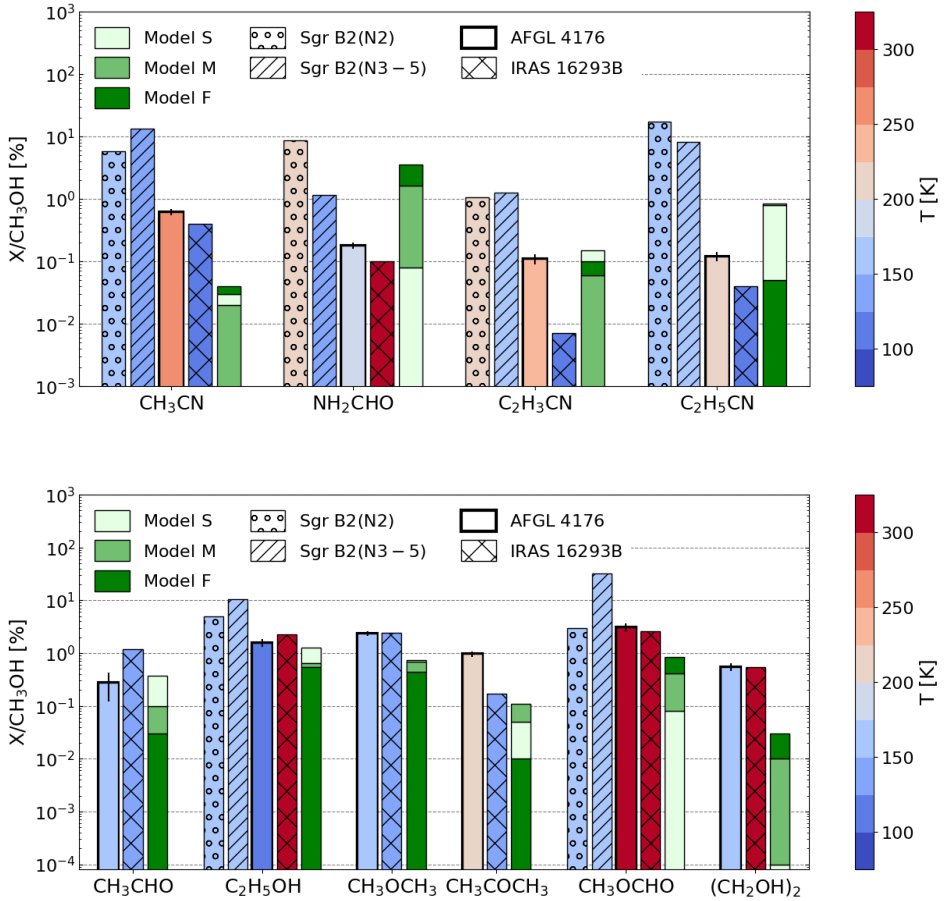


Figure 4.4: *Top panel:* Relative abundances of N-bearing species predicted by models and detected towards AFGL 4176, Sgr B2(N) and IRAS 16293B. For AFGL 4176, Sgr B2(N) and IRAS 16293B the colours of bars indicate the excitation temperature derived for each species. *Bottom panel:* Same as top panel but for O-bearing species.

With the exception of $\text{CH}_3\text{C}_2\text{H}$ and NS, all species detected towards AFGL 4176 are also detected towards Orion KL by Pagani et al. (2017), including vibrationally excited HC_3N and its ^{13}C singly substituted isotopologues. The highest energy vibrationally excited state is the $v_6 = v_7 = 1$ state, detected towards the Orion KL hot core region. In contrast, only the first two vibration states (HC_3N , $v_7=2$ and H^{13}CCCN , $v_7=1$, HC^{13}CCN , $v_7=1$ and HCC^{13}CN , $v_7=1$) were tentatively detected towards AFGL 4176.

As for AFGL 4176, both conformers of ethylene glycol are detected towards Orion KL (Favre et al., 2017). This is interesting since previously only the more stable of the two, $aGg'(\text{CH}_2\text{OH})_2$, was detected towards high-mass star-forming regions (see e.g. Lykke et al., 2015; Brouillet et al., 2015, and references therein), while the $gGg'(\text{CH}_2\text{OH})_2$ conformer was only detected towards the low-mass system IRAS 16293 (Jørgensen et al., 2016). The ratio between the aGg' and gGg' ethylene glycol conformers is 1.2 in AFGL 4176, within the errors of the value of 1.1 derived for IRAS 16293, and half the values of 2.3 and 2.5 derived for the 5 and 8 km s^{-1} components of Orion KL respectively (Favre et al., 2017).

4.4.2 Comparison with the low-mass protobinary IRAS 16293–2422

The low-mass protobinary system IRAS 16293, located at a distance of 120 pc, was observed in the ALMA Protostellar Interferometric Line Survey (PILS, see Jørgensen et al., 2016, for overview and first results). The survey covers a total of 33.7 GHz between 329 and 363 GHz with spectral and angular resolutions of 0.2 km s^{-1} and $0''.5$ (~ 60 au) respectively. The IRAS 16293 system is composed of two main components, IRAS 16293A and IRAS 16293B, with the narrow lines associated with the B source, ~ 1 km s^{-1} , making it ideal for line identification.

Of the species for which five or more lines are detected towards AFGL 4176, all have also been identified towards IRAS 16293, although $\text{CH}_3\text{C}_2\text{H}$ and NS are not reported in the PILS survey (van Dishoeck et al., 1995; Caux et al., 2011; Coutens et al., 2016; Jørgensen et al., 2016; Lykke et al., 2017; Calcutt et al., 2018; Drozdovskaya et al., 2018; Jørgensen et al., 2018). In addition, eight species with fewer than five transitions detected towards AFGL 4176 (CS and OCS only via their isotopologues) are also common between the sources. Figure 4.5 presents an overview of the relative abundances of all species detected towards AFGL 4176 and IRAS 16293B.

Overall, the composition of AFGL 4176 is more similar to that of IRAS 16293B than to the high-mass star-forming regions in the Galactic centre. Specifically, the relative column densities derived for the O-bearing species $\text{C}_2\text{H}_5\text{OH}$, CH_3OCH_3 , CH_3OCHO and $(\text{CH}_2\text{OH})_2$ towards IRAS 16293B are within a factor of two of the values derived for AFGL 4176. The remaining species show slightly larger variations with the ratio of CH_3CHO to CH_3OH being a factor of four higher in IRAS 16293B compared with AFGL 4176, and the ratio of CH_3COCH_3 to CH_3OH a factor of six lower. For N-bearing species, similar abundances are derived for CH_3CN and NH_2CHO , with variations within a factor of two between the sources. In contrast, lower ratios of both $\text{C}_2\text{H}_3\text{CN}$ and $\text{C}_2\text{H}_5\text{CN}$, are reported towards IRAS 16293B compared to AFGL 4176, by factors of 16 and three, respectively. By far the largest variations between the sources are seen in the ratios of the S-bearing species with SO_2 being close to three orders of magnitude higher in AFGL 4176 compared to IRAS 16293B, and H_2CS higher by a factor 39. However, Drozdovskaya et al. (2018) note that the SO_2 emission detected towards IRAS 16293 is likely not homogeneously distributed within the $0''.5$ PILS beam, which also misses a large extended component, and therefore the large difference between the sources could in part be explained by local variations in the distribution of the species towards IRAS 16293.

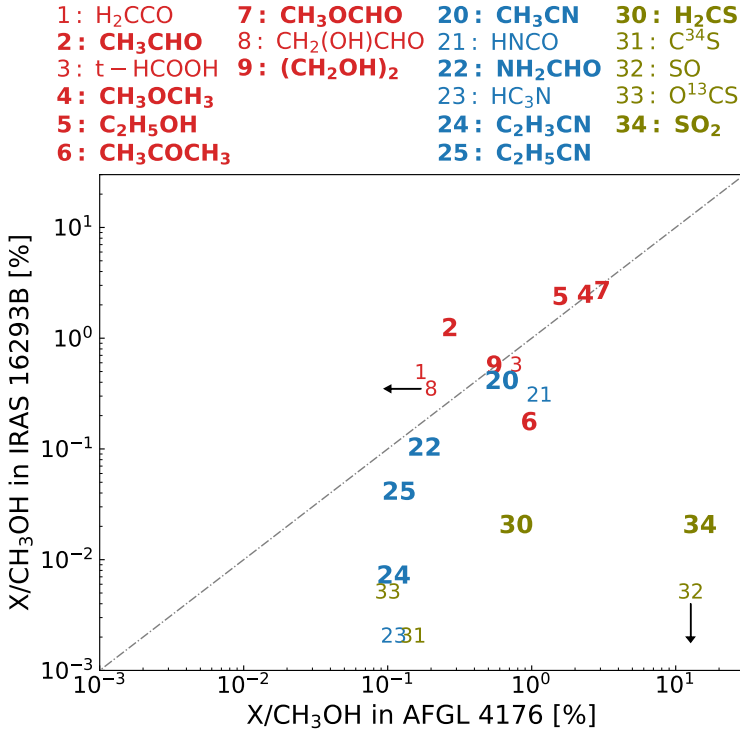


Figure 4.5: Relative abundances of species detected towards AFGL 4176 and IRAS 16293. Labels in bold refer to species with five or more detected transitions towards AFGL 4176. Oxygen-bearing species are labelled by numbers 1 through 9 in red, N-bearing species are labelled by numbers 20 through 25 in blue and S-bearing species are labelled by numbers 30 through 34 in yellow. Black arrows indicate upper limits on the relative abundance of CH₂(OH)CHO in AFGL 4176 and of SO in IRAS 16293B. The dashed grey line indicates the 1:1 ratio of relative abundances in AFGL 4176 and IRAS 16293B.

4.4.3 Comparison with chemical models

The chemistry of hot cores is commonly divided into three main phases: 1) a cold collapse phase dominated by reactions on grain surfaces involving the diffusion of light species (i.e. H); 2) a warm-up phase where relatively complex species can be formed in the ice and subsequently released into the gas phase; 3) a hot core phase dominated by gas-phase reactions triggered by the evaporation of the icy content. The models presented by Garrod (2013) couple all of these phases to trace the gas-phase, grain-surface and bulk ice chemistry throughout the evolution of the core. The physical model adopted by Garrod (2013) consists of a collapse phase followed by a gradual warm-up of the gas and dust. Three warm-up timescales are adopted: a 'fast' scale with warm-up to 200 K in 5×10^4 yr, a 'medium' scale reaching 200 K in 2×10^5 yr and a 'slow' scale taking 1×10^6 yr to reach 200 K. Listed in Table 4.5 are the predicted peak gas-phase abundance ratios for each of these models.

In the models presented by Garrod (2013), the formation of the complex O-bearing species detected in this study (i.e. CH_3CHO , $\text{C}_2\text{H}_5\text{OH}$, CH_3OCH_3 , CH_3COCH_3 , CH_3OCHO and $(\text{CH}_2\text{OH})_2$) is closely related to CH_3OH . Within the framework of the models, O-bearing species are formed primarily in warm (i.e. $30\text{ K} < T < 80\text{ K}$) ices from the recombination of radicals formed through the UV-photodissociation of CH_3OH along with other simple solid species such as H_2CO and H_2O (see also Garrod et al., 2006, 2008). While the models match the abundances of CH_3CHO , $\text{C}_2\text{H}_5\text{OH}$ and CH_3OCH_3 in AFGL 4176 within a factor of three, the abundances of CH_3COCH_3 and $(\text{CH}_2\text{OH})_2$ are underpredicted by at least an order of magnitude. For CH_3OCHO , the most abundant O-bearing species after CH_3OH , with abundances of $\sim 2\text{--}3\%$ in both AFGL 4176 and IRAS 16293B, the models predict values which are lower than the observed ones by a factor of four in the case of the fast model and a factor of 39 in the case of the slow model. A possible explanation for the mismatch between models and derived abundances of this species is poorly understood ice chemistry as well as missing gas-phase routes or included gas-phase routes which are more efficient than presumed. Indeed, a number of studies suggest that gas-phase chemistry could provide an important contribution to the formation of the molecule, either through ion-neutral or neutral-neutral reactions, following the sublimation of precursors from the ice (see e.g. Neill et al., 2011; Cole et al., 2012; Vasyunin & Herbst, 2013; Balucani et al., 2015; Taquet et al., 2016). A significant contribution from gas-phase reactions to the formation of CH_3COCH_3 , as suggested by Charnley (2001), is also possible.

The abundances of complex N-bearing species detected in this study (i.e. CH_3CN , NH_2CHO , $\text{C}_2\text{H}_3\text{CN}$ and $\text{C}_2\text{H}_5\text{CN}$) are likely the result of a combination of grain-surface and gas-phase reactions. For instance, CH_3CN can be formed on ices from the radical recombination of CH_3 and CN but also in the gas-phase via ion reactions between HCN and CH_3^+ , followed by recombination with an electron or a proton transfer reaction. In the models of Garrod (2013), CH_3CN is formed primarily in ices via $\text{CH}_3 + \text{CN} \rightarrow \text{CH}_3\text{CN}$, though a formation channel via hydrogenation of C_2N on grains at early times is also included. $\text{C}_2\text{H}_3\text{CN}$ and $\text{C}_2\text{H}_5\text{CN}$ are formed mainly during the warm-up stage as a result of a series of both gas-phase and grain-surface reactions including the formation, recombination and hydrogenation of the CN radical as well as C_2H_2 , C_2H_4 and HC_3N (Garrod et al., 2017). The formation of NH_2CHO is likely ice-dominated and proceeds via radical recombination reactions between NH_2 and HCO (e.g. Jones et al., 2011; Fedoseev et al., 2016). Alternatively, hydrogenation of HNCO may also lead to NH_2CHO . This idea is based on the strong correlation between the abundances of HNCO and NH_2CHO reported by Bisschop et al. (2007) and López-Sepulcre et al. (2015) for samples of pre-stellar and protostellar objects, indicating a connection between these species. However, such a connection contradicts the results of experimental works which show that solid-state HNCO hydrogenation does not produce NH_2CHO (Noble et al., 2015). A similar conclusion is reached by Ligterink et al. (2018b) who find that HNCO is likely not at the basis of the formation of NH_2CHO but rather formed simultaneously. Finally, a gas-phase formation route for NH_2CHO via reactions between NH_2 and H_2CO , has also been proposed (Barone et al., 2015; Codella et al., 2017).

For the detected N-bearing species, only the abundance ratio of $\text{C}_2\text{H}_3\text{CN}$ is well-matched by the models. In contrast, the abundance ratios predicted by the models for CH_3CN , NH_2CHO and $\text{C}_2\text{H}_5\text{CN}$ are all about an order of magnitude off with respect to the values derived for AFGL 4176. The abundances in AFGL 4176 do not favour either of the fast, medium or slow models over the other.

In summary, the presence of most of the detected complex molecules could be explained by warm ice chemistry triggered by UV photons. However, for some species, O- as well as N-bearing, formation routes via gas-phase reactions cannot be neglected. The chemical similarity between IRAS 16293B and AFGL 4176 suggests that the chemical composition of complex species may be set already in the cold cloud stage or that the production rates of complex species does not strongly vary with the source luminosity and might be universal in spite of the different physical conditions.

4.5 Summary

This paper presents a comprehensive study of the chemical inventory of the high-mass protostar AFGL 4176. Due to the exceptional resolving power offered by ALMA, the source is analysed on disk scales, making it possible to probe only the emission coming from the inner hot core region around the forming star while avoiding that of its large-scale cooler envelope. The source displays a rich chemistry consisting of 23 different molecular species, of which more than half, fourteen in total, are defined as complex, that is, consisting of six or more atoms. Of the detected species, the majority are oxygen-bearing while fewer contain nitrogen, sulphur or a combination thereof.

Assuming LTE, the column density is derived for all species detected towards AFGL 4176. With respect to methanol, the O-bearing species are approximately a factor of three more abundant than N-bearing species. This may indicate that AFGL 4176 is a relatively young source since nitrogen chemistry generally takes longer to evolve in the gas-phase compared with the chemistry of O-bearing species. Alternatively, if the composition of complex species is already set in the cold cloud stage, this gives an indication that formation of O-bearing species is favoured over that of N-bearing molecules. This may be due to inefficient reactions pathways (i.e. high diffusion energies and reactions barriers) for formation of N-bearing species, or due to a dominant nitrogen loss channel, for example into N₂.

With the exception of CH₃C₂H, which shows two emission peaks, the spatial distribution of N- and O-bearing species is roughly similar. Generally, all species show emission peaks near the position of the continuum peak though some O-bearing species peak up to 0''/2 away. Differences in the spatial extent of transitions of the same species with low and high E_{up} are seen for the majority of species. For a number of species a velocity gradient is detected across the source consistent with the Keplerian-like disk reported by Johnston et al. (2015).

Overall, the chemical composition of AFGL 4176 is more similar to that of the low-mass protostar IRAS 16293B than to that of the high-mass star-forming region Sgr B2(N). Taking methanol as a reference, the abundances of C₂H₅OH, CH₃OCH₃, CH₃OCHO and (CH₂OH)₂ in IRAS 16293B are within a factor of two of the abundances in AFGL 4176. In contrast, the C₂H₅OH/CH₃OH and CH₃OCHO/CH₃OH values derived for Sgr B2(N) are higher than those in AFGL 4176 by up to an order of magnitude. For the N-bearing species, the abundances of CH₃CN, C₂H₅CN and NH₂CHO are similar between AFGL4176 and IRAS 16293B while C₂H₃CN/CH₃OH is lower by a factor of 16 in IRAS 16293B. For Sgr B2(N) the abundances of all N-bearing species are significantly higher than in AFGL 4176. The similarity between abundances in AFGL 4176 and IRAS 16293B indicates that the production of complex species does not depend strongly on the luminosity of sources, but may be universal despite differences in physical conditions or that the composition of species is set already in the ice during the cold cloud stage.

Acknowledgements. This paper makes use of the following ALMA data: ADS/JAO.ALMA #2012.1.00469.S. ALMA is a partnership of ESO (representing its member states), NSF (USA) and NINS (Japan), together with NRC (Canada) and NSC and ASIAA (Taiwan) and KASI (Republic of Korea), in cooperation with the Republic of Chile. The Joint ALMA Observatory is operated by ESO, AUI/NRAO and NAOJ. This work is based on analysis carried out with the CASSIS software and JPL: <http://spec.jpl.nasa.gov/> and CDMS: <http://www.ph1.uni-koeln.de/cdms/> spectroscopic databases. CASSIS has been developed by IRAP-UPS/CNRS (<http://cassis.irap.omp.eu>).

Appendix A: Model grids

Table A.1: Overview of model grids

N_s range [cm^{-2}]	Species	N_s range [cm^{-2}]	Species
$10^{15} - 10^{16}$	$\text{C}_2\text{H}_3\text{CN}$	$5 \times 10^{16} - 5 \times 10^{17}$	$^{13}\text{CH}_3\text{OH}$
$5 \times 10^{15} - 5 \times 10^{16}$	CH_3CHO NH_2CHO		CH_3OCH_3 CH_3OCHO
$10^{16} - 10^{17}$	$\text{CH}_3\text{C}_2\text{H}$ CH_3CN $\text{CH}_3\text{CN}, \nu_8=1$ H_2CS $(\text{CH}_2\text{OH})_2$	$10^{16} - 5 \times 10^{17}$	$\text{C}_2\text{H}_5\text{OH}$
		$5 \times 10^{17} - 5 \times 10^{18}$	SO_2

Notes. All grids have T_{ex} spanning 50 – 500 K in steps of 10 K and N_s sampled by 20 logarithmically spaced steps, apart from the grid for $\text{C}_2\text{H}_5\text{OH}$ which has 30 logarithmically spaced steps.

Appendix B: Unidentified lines

Table B.1: List of unidentified lines

Rest frequency ^a [GHz]	Peak intensity [K]
238.806	1.9
239.078	4.2
239.082	3.6
239.651	1.9
239.655	2.7
239.926	1.9
240.129	2.0

Continued on next page

Continued from previous page

Rest frequency ^a [GHz]	Peak intensity [K]
240.132	2.0
240.155	2.1
240.517	2.5
240.562	2.0
240.565	2.2
240.574	1.9
240.579	2.2
240.702	2.1
240.718	2.0
240.753	2.0
241.102	1.4
241.127	1.5
<hr/>	
254.192	2.9
254.340	2.0
254.346	2.6
254.581	3.9
254.669	3.0
254.686	7.0
254.713	5.7
254.716	5.2
254.858	4.6
<hr/>	
256.107	3.8
256.111	3.8

Notes. ^(a) Assuming $v_{\text{LSR}} = -53.5 \text{ km s}^{-1}$ for AFGL 4176.

Appendix C: Full model

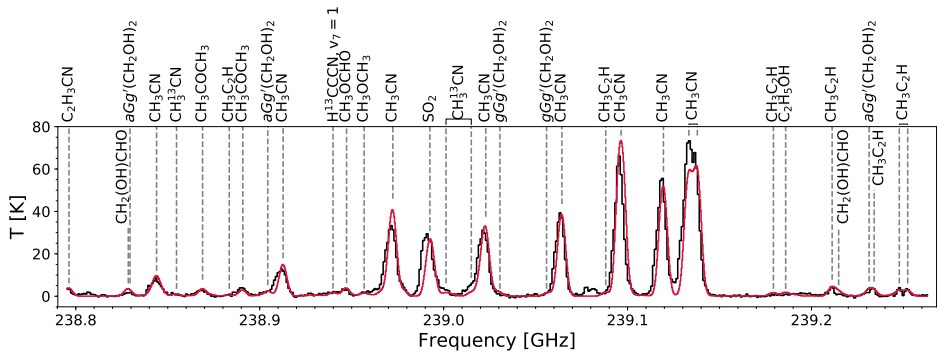


Figure C.1: Same as Fig. 4.2 for species detected towards AFGL 4176 in the spectral window centred at 239.0 GHz.

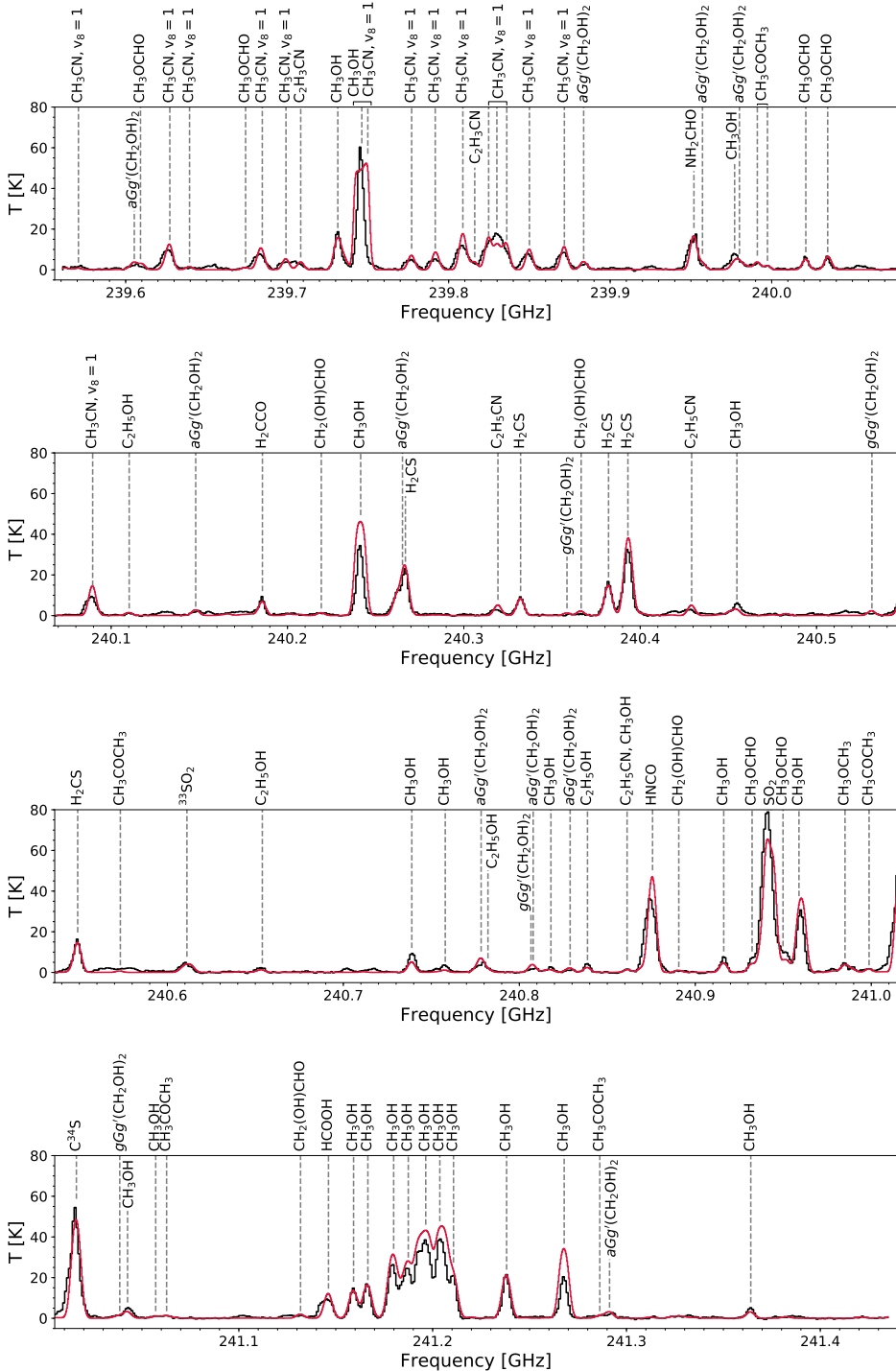


Figure C.2: Same as Fig. 4.2 for species detected towards AFGL 4176 in the spectral window centred at 240.5 GHz.

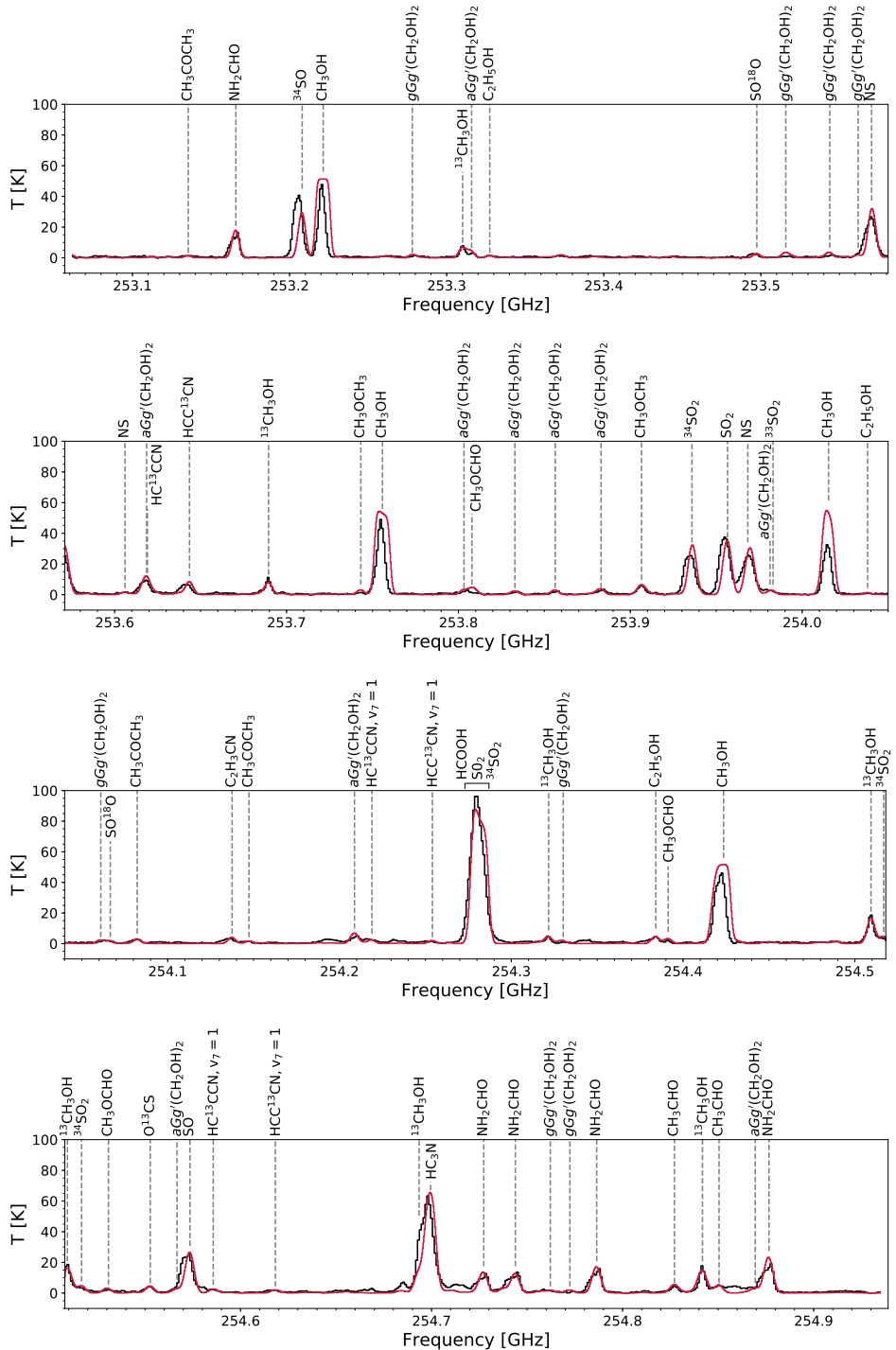


Figure C.3: Same as Fig. 4.2 for species detected towards AFGL 4176 in the spectral window centred at 254.0 GHz.

Appendix D: Line maps

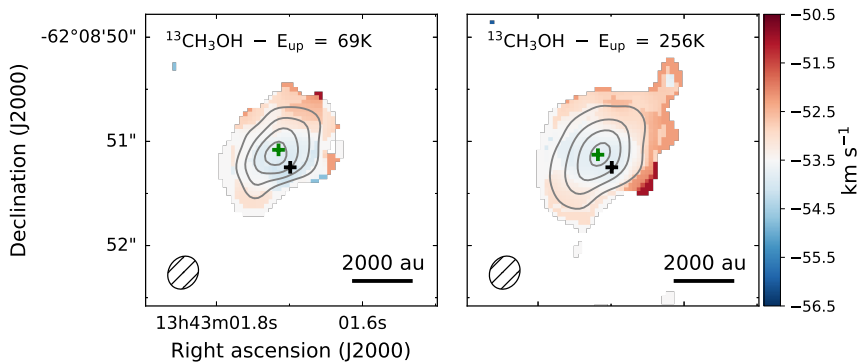


Figure D.1: Same as Fig. 4.3 for $^{13}\text{CH}_3\text{OH}$ lines at 256.1716 GHz (left) and 253.6895 GHz (right). Contours start at 9σ and are in steps of 6σ and 12σ , with $\sigma = 6.27 \times 10^{-3}$ and $6.87 \times 10^{-3} \text{ Jy beam}^{-1} \text{ km s}^{-1}$, for the left and right panel, respectively.

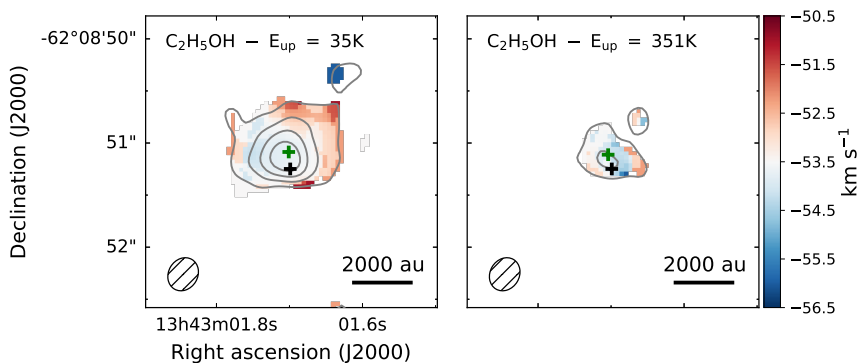


Figure D.2: Same as Fig. 4.3 for $\text{C}_2\text{H}_5\text{OH}$ lines at 254.3841 GHz (left) and 253.3274 GHz (right). Contours start at 3σ and are in steps of 6σ , with $\sigma = 5.58 \times 10^{-3}$ and $5.39 \times 10^{-3} \text{ Jy beam}^{-1} \text{ km s}^{-1}$, for the left and right panel, respectively.

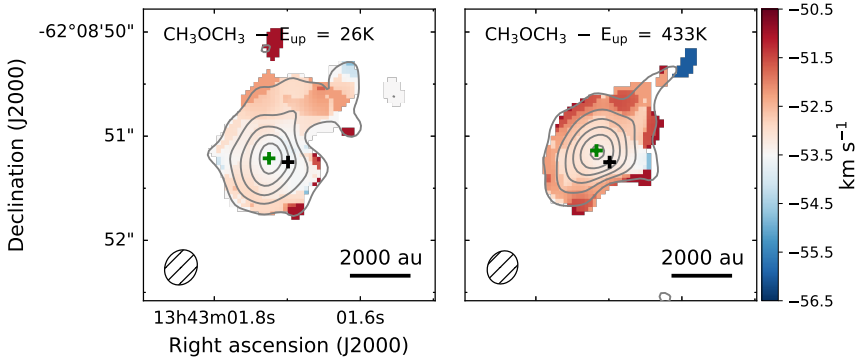


Figure D.3: Same as Fig. 4.3 for CH_3OCH_3 lines at 240.9851 GHz (left) and 253.9075 GHz (right). Contours start at 3σ and are in steps of 6σ , with $\sigma = 4.95 \times 10^{-3}$ and 6.08×10^{-3} $\text{Jy beam}^{-1} \text{ km s}^{-1}$, for the left and right panel, respectively.

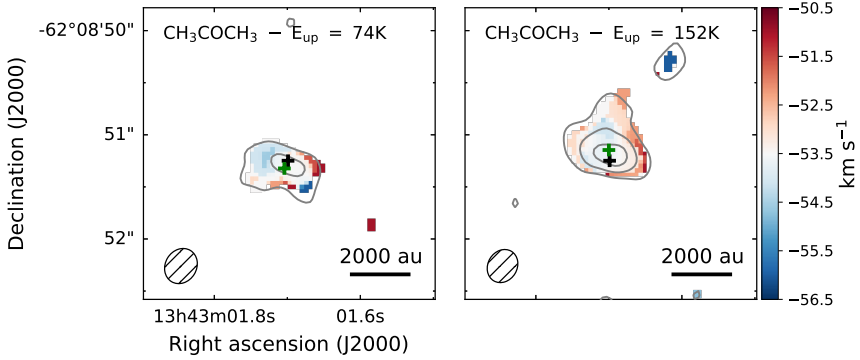


Figure D.4: Same as Fig. 4.3 for CH_3COCH_3 lines at 240.9988 GHz (left) and 254.0822 GHz (right). Contours start at 3σ and are in steps of 6σ , with $\sigma = 4.96 \times 10^{-3}$ and 5.32×10^{-3} $\text{Jy beam}^{-1} \text{ km s}^{-1}$, for the left and right panel, respectively.

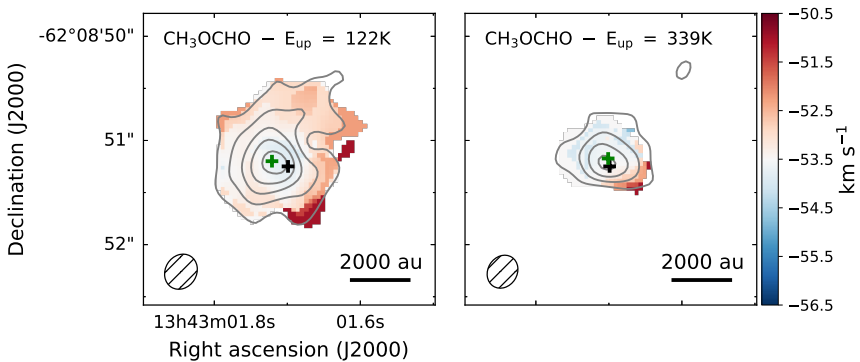


Figure D.5: Same as Fig. 4.3 for CH_3OCHO lines at 240.0211 GHz (left) and 256.4478 GHz (right). Contours start at 3σ and are in steps of 6σ , with $\sigma = 5.36 \times 10^{-3}$ and 5.96×10^{-3} $\text{Jy beam}^{-1} \text{ km s}^{-1}$, for the left and right panel, respectively.

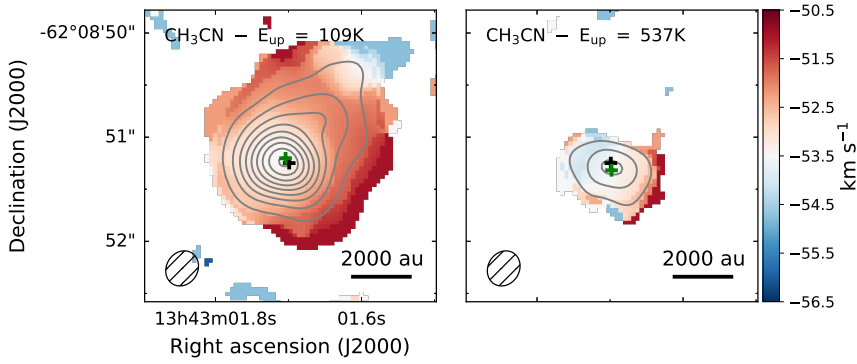


Figure D.6: Same as Fig. 4.3 for CH_3CN lines at 239.0965 GHz (left) and 238.8439 GHz (right). Contours start at 9σ and are in steps of 12σ , with $\sigma = 1.26 \times 10^{-2}$ and $5.78 \times 10^{-3} \text{ Jy beam}^{-1} \text{ km s}^{-1}$, for the left and right panel, respectively.

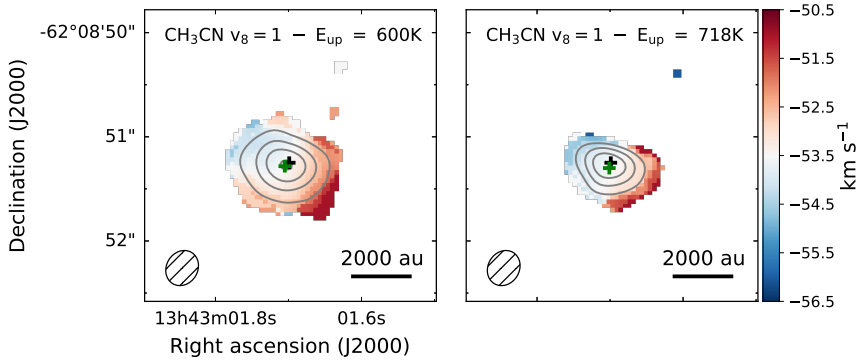


Figure D.7: Same as Fig. 4.3 for vibrationally excited CH_3CN lines at 240.0895 GHz (left) and 239.7917 GHz (right). Contours start at 9σ and are in steps of 12σ and 6σ for the left and right panel, respectively, with $\sigma = 5.41 \times 10^{-3} \text{ Jy beam}^{-1} \text{ km s}^{-1}$.

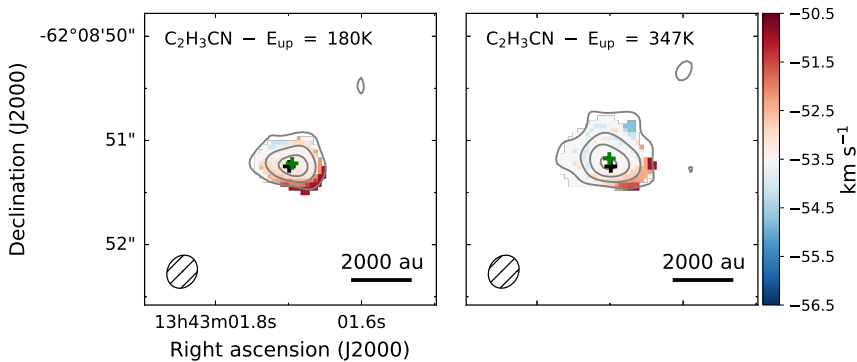


Figure D.8: Same as Fig. 4.3 for $\text{C}_2\text{H}_3\text{CN}$ lines at 254.1375 GHz (left) and 256.4480 GHz (right). Contours start at 3σ and are in steps of 6σ , with $\sigma = 5.29 \times 10^{-3}$ and $6.0 \times 10^{-3} \text{ Jy beam}^{-1} \text{ km s}^{-1}$, for the left and right panel, respectively.

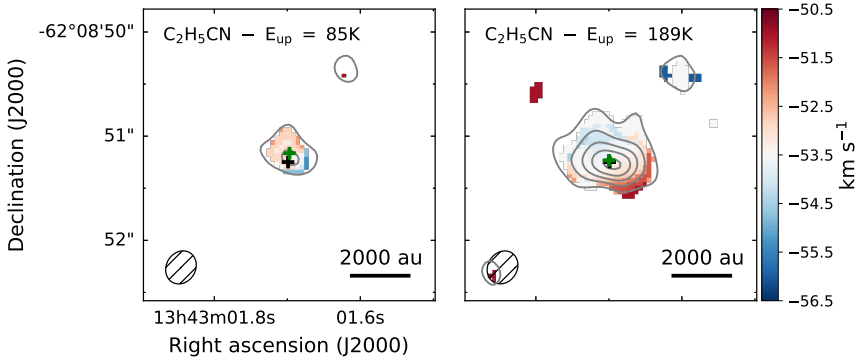


Figure D.9: Same as Fig. 4.3 for C₂H₅CN lines at 254.6336 GHz (left) and 256.3959 GHz (right). Contours start at 3σ and are in steps of 6σ , with $\sigma = 5.18 \times 10^{-3}$ and 5.7×10^{-3} Jy beam⁻¹ km s⁻¹, for the left and right panel, respectively.

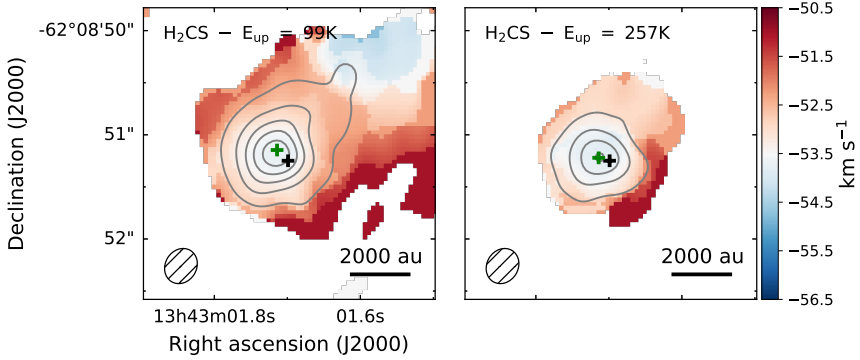


Figure D.10: Same as Fig. 4.3 for H₂CS lines at 240.5491 GHz (left) and 240.3322 GHz (right). Contours start at 9σ and are in steps of 12σ , with $\sigma = 6.81 \times 10^{-3}$ and 5.27×10^{-3} Jy beam⁻¹ km s⁻¹, for the left and right panel, respectively.

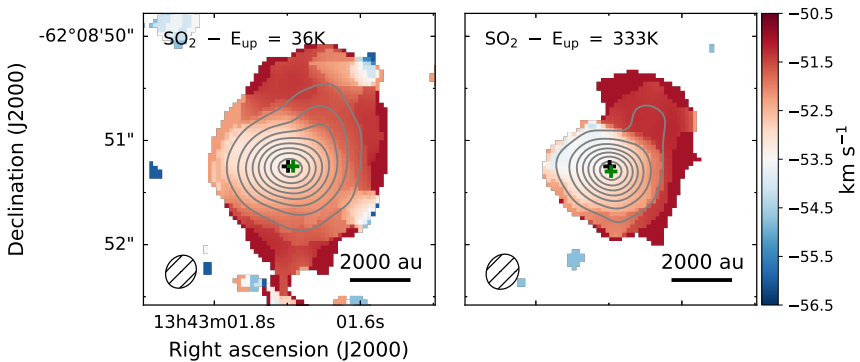


Figure D.11: Same as Fig. 4.3 for SO₂ lines at 256.2469 GHz (left) and 238.9925 GHz (right). Contours start at 9σ and are in steps of 12σ , with $\sigma = 1.96 \times 10^{-2}$ and 8.63×10^{-3} Jy beam⁻¹ km s⁻¹, for the left and right panel, respectively.